

Synchrotron X-ray imaging in 4D: Multiscale failure and compaction localization in triaxially compressed porous limestone

Lingcao Huang, Patrick Baud, Benoit Cordonnier, François Renard, Lin Liu, Teng-Fong Wong

▶ **To cite this version:**

Lingcao Huang, Patrick Baud, Benoit Cordonnier, François Renard, Lin Liu, et al.. Synchrotron X-ray imaging in 4D: Multiscale failure and compaction localization in triaxially compressed porous limestone. Earth and Planetary Science Letters, 2019, 528, pp.115831. 10.1016/j.epsl.2019.115831 . hal-02334959

HAL Id: hal-02334959
https://hal.science/hal-02334959

Submitted on 21 Dec 2021

HAL is a multi-disciplinary open access archive for the deposit and dissemination of scientific research documents, whether they are published or not. The documents may come from teaching and research institutions in France or abroad, or from public or private research centers.

L'archive ouverte pluridisciplinaire **HAL**, est destinée au dépôt et à la diffusion de documents scientifiques de niveau recherche, publiés ou non, émanant des établissements d'enseignement et de recherche français ou étrangers, des laboratoires publics ou privés.



Distributed under a Creative Commons Attribution - NonCommercial 4.0 International License

Version of Record: https://www.sciencedirect.com/science/article/pii/S0012821X19305230
Manuscript_8e0eaeb2d57850459cad77aaee44ccc3

Synchrotron X-ray imaging in 4D: Multiscale failure and compaction localization in triaxially compressed porous limestone

Lingcao Huang [a], Patrick Baud [b*], Benoit Cordonnier [c,d], François Renard [c,e], Lin Liu [a], Teng-fong Wong[a]

[a] *Earth System Science Programme, Faculty of Science, The Chinese University of Hong Kong, Hong Kong*

[b] *Institut de Physique du Globe de Strasbourg (UMR 7516 CNRS, Université de Strasbourg/EOST,) France (patrick.baud@unistra.fr)*

[c] *Departments of Geosciences and Physics, The Njord Centre, University of Oslo, Norway*

[d] *ESRF, The European Synchrotron, CS40220, Grenob1e 38043, France*

[e] *Univ. Grenoble Alpes, Univ. Savoie Mont Blanc, CNRS, IRD, IFSTTAR, ISTerre, 38000 Grenoble, France*

ABSTRACT

Understanding failure and strain localization in porous rock is of fundamental importance in rock physics. Confined compaction experiments on porous rocks have revealed a broad spectrum of failure modes. Techniques such as acoustic emission location and velocity tomography provide kinematic information on the partitioning of damage and localization of strain. Complementary observations on deformed samples using microscopy and microcomputed tomography (μCT) can also be used to image microscale damage and its distribution. Only by synthesizing such measurements on multiple scales could one infer the multiscale dynamics of compaction localization and similar rock failure phenomena. Located at the European Synchrotron Radiation Facility, the HADES rig allows direct *in situ* 3D imaging of the whole rock sample as it is triaxially compressed. The μCT data provide an integrated perspective of the spatiotemporal evolution of damage and strain localization on scales ranging from grain to continuum. We conducted an experiment on Leitha limestone (initial porosity of ~22%) at a confining pressure

© 2019 published by Elsevier. This manuscript is made available under the CC BY NC user license
https://creativecommons.org/licenses/by-nc/4.0/

of 20 MPa. With increasing differential stress, the sample strain hardened and two distinct yield points were identified in the stress-strain curve. The spatiotemporal evolution of local porosity and damage were analyzed at multiple scales. At a mesoscopic scale of 10 voxels (65 μm), the time-lapse μCT images reveal the strain partitioning associated with the first yield point and development of strain localization with the second. The latter development of five discrete compaction bands is the first unambiguous observation of such a bifurcation phenomenon in a porous carbonate rock, with geometric attributes comparable to compactions bands observed in porous sandstones. The μCT data on the voxel-scale elucidate in refined details the nucleation and propagation of discrete compaction bands under quasi-static loading, as well as the micromechanical processes, which in the past can only be inferred from a synthesis of kinematic observations of acoustic emissions activity and post-mortem observations of microstructure and damage.

Keywords: limestone deformation, bifurcation, compaction bands, X-ray microtomography.

1. Introduction

Mechanical failure in the Earth's crust is often accompanied by localization of strain that ranges in scale from hand specimens to zones of hundreds of kilometres. Crustal rock has pore space made up of numerous elongate microcracks and equant pores. Under an applied stress field, damage develops on the grain scale by growth of microcracks and collapse of pores. Initially such damages proliferate in a distributed manner, but at higher stresses a subset may coalesce to constitute a localized zone of intense deformation, which extends over multiple grains and ultimately cuts through an experimental sample (e.g. Passchier and Trouw, 2005; Paterson and Wong, 2005). In the field this process of strain localization cascades and extends in scale from cm to hundreds of kilometres (Anders et al., 2015; Fossen et al., 2017).

Accordingly the phenomenon of strain localization is intrinsically a multiscale process, a fundamental understanding of which hinges on integrated characterization of the spatiotemporal development of damage from the grain to continuum scale. In a compact rock, compressive failure typically involves brittle faulting accompanied by the localization of shear strain. Acoustic emissions (AE) have been effective as proxies for the grain-scale damage related to faulting. By locating the AE activity of a Westerly granite sample as it failed progressively under quasistatic loading, Lockner et al. (1992) were able to elucidate the spatiotemporal development of shear localization on the continuum scale. By analyzing the AE waveforms from multiple receivers, one can broadly categorize the mechanism of an event as implosive, shear or tensile (e.g., Zang et al., 2000), but further details of the grain-scale micromechanical processes can only be acquired by systematic microscopy on the deformed samples (e.g., Wong, 1982; Moore and Lockner, 1995).

In a porous rock compressive failure by brittle faulting is commonly observed, accompanied also by shear localization. However, field and laboratory studies in the past two decades have documented a fundamentally different mode of strain localization in porous rocks under high confinement. Failure in this mode derives from cataclastic compaction that localizes in a planar structure (compaction band, CB) oriented sub-perpendicular to the maximum compressive stress (Mollema and Antonellini, 1996; Olsson, 1999). These CBs may develop as multiple discrete bands (Wong et al., 2001; Baud et al., 2004), or as a diffuse band that widens with progressive deformation (Olsson and Holcomb, 2000). In the laboratory, compaction band formation is accompanied by significant permeability reduction (Vajdova et al., 2004; Baud et al., 2012), whereas field observations and numerical simulations have highlighted potentially significant impacts on fluid flow at the reservoir and aquifer scale (e.g., Sternlof et al., 2004).

Some of the most comprehensive investigations in the field and laboratory of this phenomenon of compaction localization have been on porous sandstone (Fortin et al., 2005; Tembe et al., 2008; Eichhubl et al., 2010; Fossen et al., 2011). Again AE measurements in the laboratory have been effective in mapping out the spatiotemporal development of both discrete and diffuse CBs (Olsson and Holcomb, 2000; Fortin et al., 2006; Townend et al., 2008). Only when these kinematic data on damage development on the continuum scale are synthesized with microstructural observations including X-ray computed tomography (CT) in 3D imaging (Louis et al., 2006; Baud et al., 2015), can one arrive at a consistent description of the multiscale mechanics of compaction localization. Ideally one would like to be able to acquire data on multiple scales on a single sample, so as to resolve details on the dynamical development. How did a CB nucleate and what micromechanical processes trigger the bifurcation in strain? It is likely that the nucleation is from a preexisting local heterogeneity in the pore space or rock

matrix. What is the scale of the heterogeneity? For Bleurswiller sandstone Fortin et al. (2006) inferred from their AE and CT data that relatively large heterogeneities in the form of "porosity patches" provided nucleation sites for CBs, but Baud et al. (2015) argued that there is no causal relation between collapse of these patches and CB formation.

In comparison, compaction localization in other porous rocks has not been investigated in as much detail. In carbonate rocks, diffuse CBs have been reported in laboratory deformed samples of calcarenite (Baxevanis et al., 2006) and Leitha limestone (Baud et al., 2017a). Microstructural signatures of strain localization in porous limestones are subtle and not readily resolved under either optical or electron microscopes (Ji et al., 2015). The use of AE for monitoring damage development is limited by the typically low AE activity in calcitic rock (Vajdova et al., 2004; Schubnel et al., 2006). Nevertheless, for the Saint-Maximin limestone Baud et al. (2017b) observed significant AE activity likely related to microcracking at the quartz grain interfaces, but according to microstructural observations, the dominant micromechanical process for compaction was pore collapse, which seemed to be ineffective in generating AE. Spatial distribution of AE in this quartz-rich limestone underscores the development of "complex diffuse compaction bands" at high confinement. Accordingly these observations seem to indicate that CBs in a carbonate rock tend to develop in a diffuse manner, which leads to the following question: Can discrete CBs develop in a carbonate rock, and if not, what are the microstructural attributes that inhibit their development?

The use of time-lapse 3D imaging by X-ray CT has opened up the possibility of characterizing in situ the compressive failure of geomaterials (Lenoir et al., 2007; Andò et al., 2012; Fusseis et al., 2013; Zhao et al., 2018). In particular, Renard et al. (2016, 2017) recently developed a triaxial deformation apparatus that is transparent to the high flux of X-rays of a

synchrotron, which can potentially elucidate the multiscale failure of a crustal rock under elevated pressures and temperatures. With a spatial resolution of several microns, the apparatus furnishes 4D imaging of a centimeter-size sample loaded quasistatically in triaxial compression, which delineates the progressive development of failure and strain localization from the grain to continuum scale. In this study we leverage this advance in experimentation to tackle the several questions outlined above, in relation to the development of compaction localization in the Leitha limestone.

2. Materials and Methods

A cylindrical core (5 mm in diameter and 10 mm in height) of Leitha limestone was cored orthogonal to the sedimentary bedding from a block collected in the quarry Hummel St. Margarethen/ Burgenland near Vienna (Austria). The Leitha limestone is a carbonate grainstone composed of > 99% calcite, and occurs with a broad range of grain sizes and porosity, related to changes in depositional regime and degree of cementation (Rath et al., 2011). Baud et al. (2017b) performed detailed microstructural analysis and X-ray CT imaging on samples with porosity between 18% and 31%. They showed that Leitha limestone is essentially an aggregate of cemented bioclasts of relatively homogeneous size, and the pore space of samples from our block is dominated by macropores of relatively large size (with average around 165 μm).

Several other samples were cored for porosity measurement and additional mechanical tests. With a helium pycnometer the porosity of a sample (20 mm in diameter and 40 mm in height) that had been dried *in vacuo* for 48h was determined to be 26%, in agreement with another

estimation based on the bulk density of the sample and assuming that the studied rock is made of 100% of calcite.

The experiment was conducted at the European Synchrotron Radiation Facility (ESRF) in Grenoble, France, using the triaxial compression apparatus, HADES (Renard et al., 2016) installed on an X-ray μCT rotation stage at beamline ID19. The sample was jacketed with Viton, and confining medium was silicon oil. A confining pressure up to 100 MPa can be generated, with a maximal uncertainty of 0.05 MPa. The differential stress up to a maximum value of 200 MPa was independently applied. The axial displacement was monitored with a displacement transducer (LVDT), with a precision of 3 μm.

The experiment was conducted on the nominally dry sample at room temperature. A hydrostatic stress of 20 MPa was first applied, and before the application of differential stress, the first X-ray tomography scan was acquired. Made of titanium, the body of the triaxial rig is transparent to X-rays from the synchrotron source (with estimated equivalent beam energy of 85 keV). Keeping confining pressure fixed at 20 MPa, the axial piston was progressively advanced by increments of 1-2 MPa. After each step in stress, the differential stress was held constant as the apparatus was rotated over 180°, while 1,800 X-ray radiographs were acquired with a voxel size of 6.5μm. The radiograph extended over 13x13 mm^2 (2000x2000 voxels), covering full length and width of sample and parts of the pistons and confining medium. Durations of the stress step and tomography scan were 1-2 minutes and 3 minutes, respectively. Reconstruction of the 3D volumes from the radiographs was performed at beamline ID19 at the ESRF, using both X-ray adsorption and phase contrast imaging (Mirone et al., 2014).

First-order characteristics of the pore space can be inferred from the global histogram of the X-ray attenuation coefficient mapped onto a gray level. Fig. S1 shows the 16-bit data for our limestone sample at differential stresses of 4, 55 and 74 MPa. In each histogram one can readily recognize two distinct modes, with relatively symmetric distributions on either side of the peaks. The area under the first peak decreases with increasing compaction. The two modes are separated by a broad range of gray level, with a well-defined intermodal valley in between. Guided by our previous microstructural observations (Baud et al., 2017a) and macroscopic measurement of porosity, we binarized the CT-images by selecting a fixed gray level (9500) as the threshold for segmentation, such that the void and solid domains correspond to voxels with gray levels below or above this threshold. It should be noted that we were able to adopt this simple protocol for segmentation only because the pore space of our Leitha limestone sample was dominated by macropores, with minimal microporosity. In most limestones with significant fractions of dual porosities, the intermodal valley is not as well-defined, and more elaborate protocols are necessary for segmentation (Ji et al., 2012).

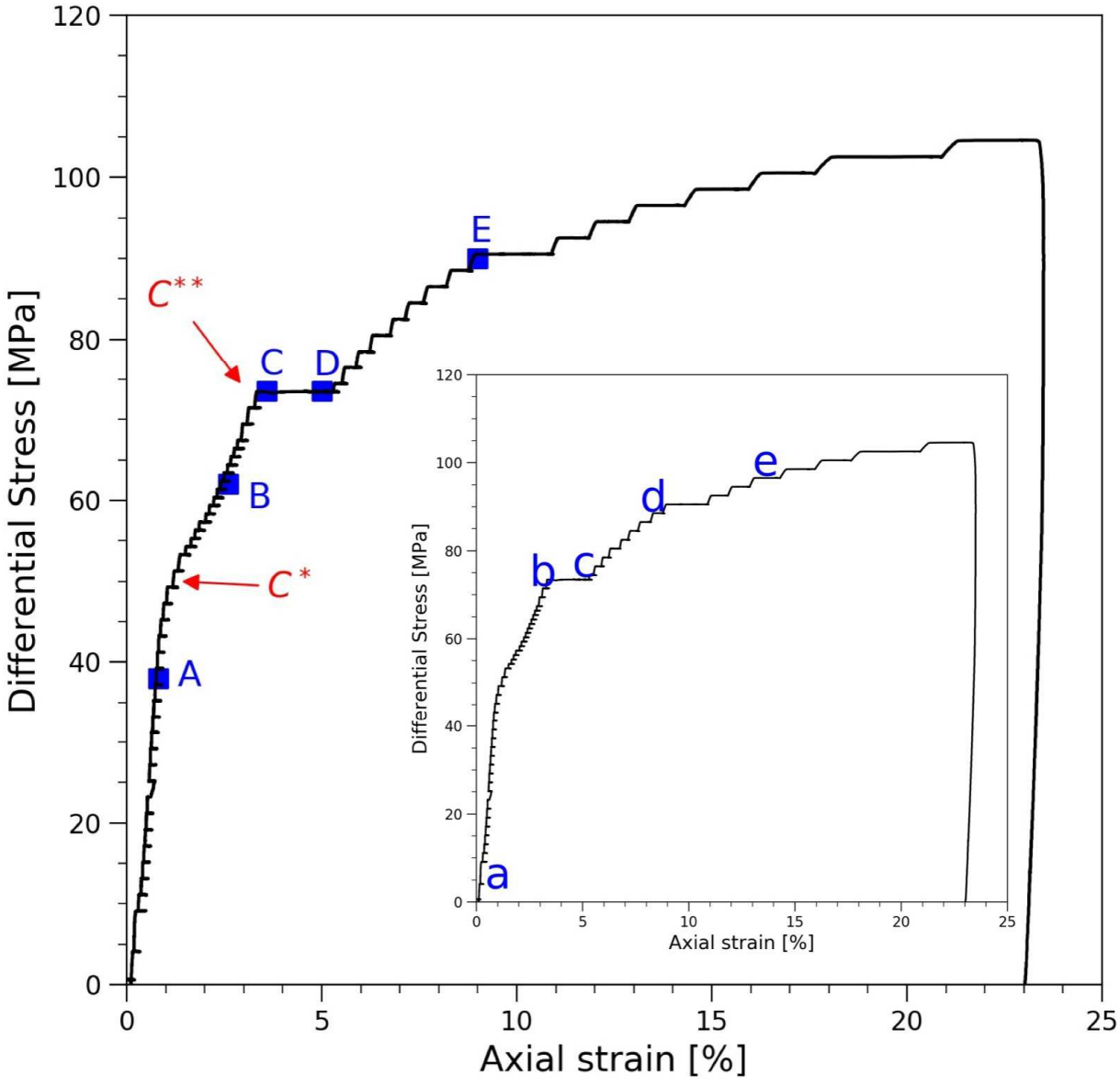
3. Results

3.1. Mechanical deformation and failure mode

We present in Fig. 1 the mechanical data, with the differential stress as a function of axial strain (shortening measured from LVDT divided by the nominal sample length). The differential stress increased monotonically to a level of 104 MPa, as the sample accumulated an axial strain of more than 20% before it collapsed catastrophically. Two notable changes in the slope of the stress-strain curve were observed at differential stresses of 50 MPa and 73 MPa, marked by C^*

178 and *C*** in the Fig. 1, respectively. We will argue later that the sample underwent two stages of
179 yielding associated with these two critical stresses. We also present videos S2 and S3, which are
180 time-lapse radiographs of two orthogonal axial sections (R0 and R90) of the sample acquired in
181 the experiment.

182



183
184
185

Fig. 1. Mechanical data for a sample of Leitha limestone deformed at a confining pressure of 20 MPa. Differential stress is plotted as a function of axial strain. The critical stresses *C** and *C*** are indicated by red arrows. The steps (A, B, C, D, E) for the five scans in Fig.4a are marked on the stress-strain curve. Similarly the steps (a, b, c, d, e) for the micrographs in Fig.7, Fig.8 and Fig. 9 are marked on the inset stress-strain curve.

The radiographs at four stress levels were selected to highlight the progressive development of damage as seen in the videos. At a low differential stress of 11 MPa (and confining pressure of 20 MPa), the sample sustained mostly elastic deformation and its pore space is likely similar to the undeformed state. The orthogonal radiographs (Fig. 2a) show that this initial distribution of porosity was quite heterogeneous, and in particular, a large cluster of macropores can be seen within a top layer (bracketed by the two white dashed lines). At a stress of 66 MPa (well beyond *C** but before *C***), this macropore cluster and other pores in the top layer have compacted significantly. Nevertheless deformation in this layer appears distributed, in that the large and small pores both seem to have sustained comparable compaction. In contrast, the lower two-third of the sample showed minimal compaction (Fig. 2a and 2b).

Fig. 2c was acquired at a stress of 74 MPa after the sample had sustained an overall strain of ~2% beyond *C***. Most of the pores had contracted to a degree, but the most intense compaction developed preferentially within a layer bracketed by the white dashed lines in the lower half of the sample. As the sample strain hardened to a stress of 96 MPa and accumulated an overall strain of 15%, compaction appeared to have preferentially developed in a somewhat thicker layer (bracketed by white lines in Fig. 2d). If these were the only micrographs of the deformed sample available, the likely interpretation would be that these layers in Fig. 2c and 2d correspond to the widening of a diffuse CB. However, our latter analysis will reveal that this interpretation is overly simplistic. It should also be noted that our sample at the highly deformed stages did not

show any sign of asymmetric bulging, which would have indicated the development of shear localization.

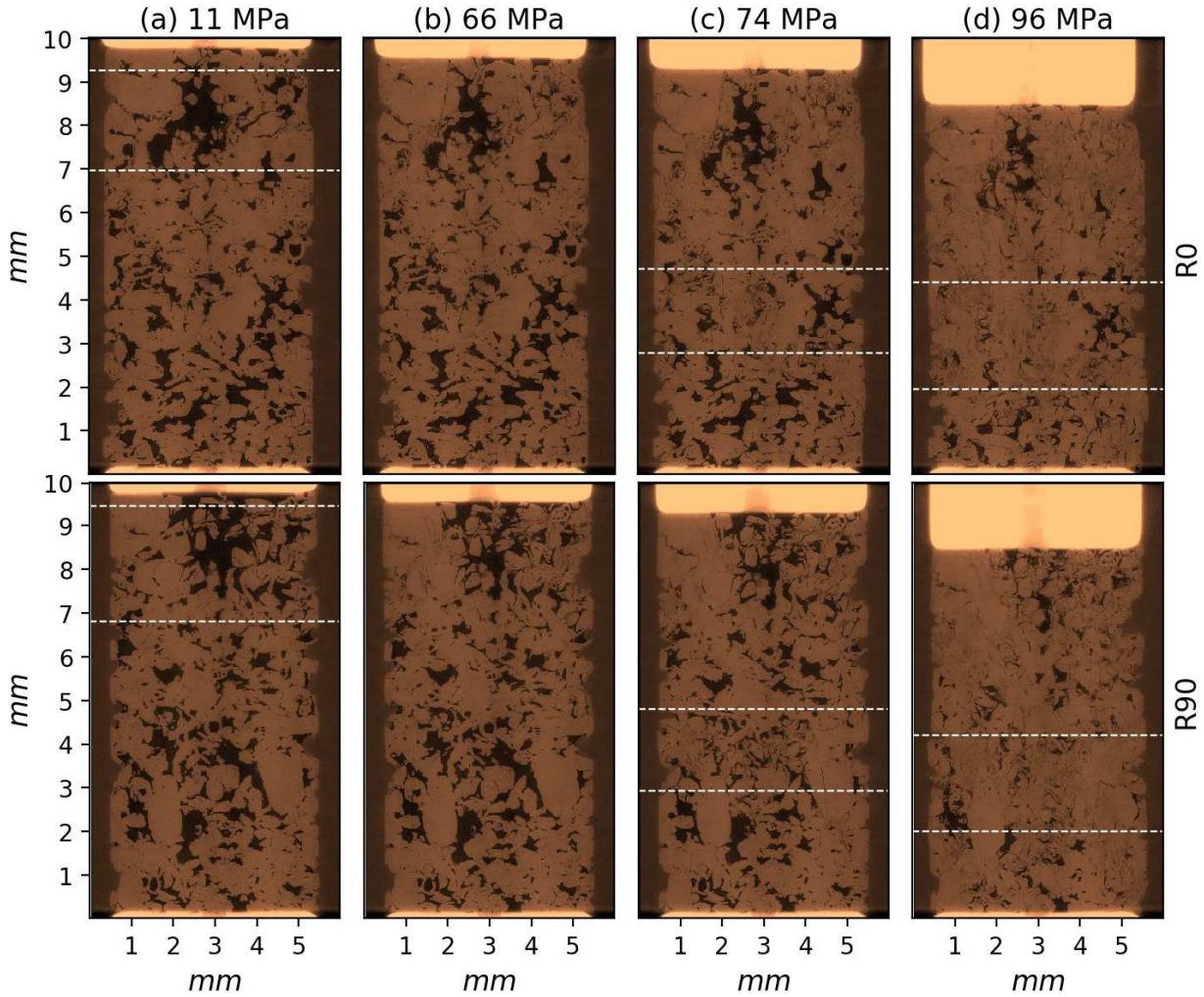


Fig. 2. Radiographs of two orthogonal sections (R0 and R90) at (a) 11, (b) 66, (c) 74, and (d) 96 MPa of differential stress.

3.2. Strain partitioning and compaction localization

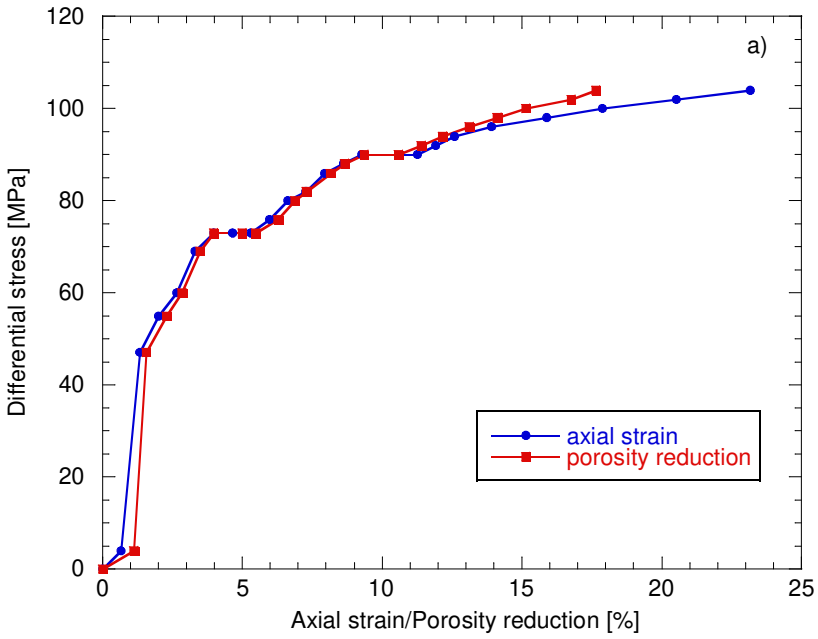
The 4D imaging allows us to characterize the deformation from the sample scale down to voxel scale. This is tackled first using the segmented images. With reference to the grayscale threshold (Fig. S1), all the CT images were segmented into solid and void domains. The standard protocol in microstructural analysis is to exclude regions in the vicinity of the jacket and loading

223 pistons, to circumvent artifacts induced by local stress anomalies and end effects. We adopted
224 the same approach, masking such regions in our analysis. The diameter was reduced from 5 mm
225 to 4.55 mm (700 voxels) in the masked segmented images. Two layers of thickness 0.13 mm (20
226 voxels) were masked in the immediate vicinity of the top and bottom pistons, respectively.

227 At the sample scale the porosity ϕ of our segmented CT images had an initial value of 22.5%
228 at confining pressure of 20 MPa. As noted earlier the porosity of a larger sample under ambient
229 pressure was determined to be 26%, and the apparent discrepancy can be attributed to several
230 factors. First is compaction due to the hydrostatic confinement. Second, a disproportionate
231 number of macropores were observed in the masked region near the sample ends and surface,
232 which were excluded in our analysis. Third, there could be pores smaller than the voxel
233 dimension of 6.5 μm not resolved in the μCT images.

234 The peak differential stress attained in the experiment was 104 MPa, and by then most of the
235 porosity was eliminated down to 4.8% (Fig. 3a). On the μCT images we can determine the axial
236 shortening from the change in piston positions and divide it by the initial length, thus arriving at
237 an independent measure of the axial strain ε, which is plotted in Fig. 3a and shown to be in good
238 agreement with the LVDT data in Fig. 1. Interestingly our data show that the porosity reduction
239 $\Delta\phi$ and axial strain ε basically coincided during most of the experiment up to about 15% of axial
240 strain, with the implication that although the limestone sample was compressed triaxially,
241 negligible deformation developed in the transverse direction such that the axial strain was
242 essentially taken up by a corresponding reduction in porosity. The absence of dilatancy during
243 triaxial compression also suggests that dilatant failure by shear faulting was unlikely. According
244 to bifurcation analysis of strain localization, such a deformation field is favorable for CB

formation (Rudnicki, 2004). Baud et al. (2004) also showed that CBs in Bentheim sandstone developed with negligible radial strain.



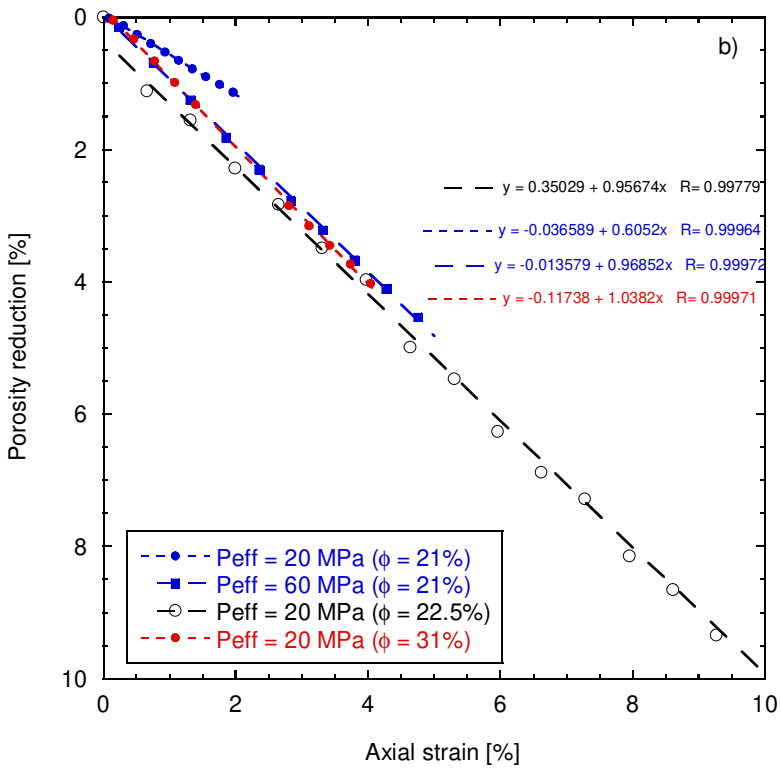


Fig. 3. (a) Differential stress as a function of axial strain (blue) and porosity reduction (red), both calculated from the CT images, for the sample deformed in this study at a confining pressure of 20 MPa. (b) Compilation of data on Leitha limestone. Porosity reduction is plotted as a function of axial strain for samples of starting porosity 21% (red), and 31% (blue) deformed by Baud et al. (2017a) in wet conditions at different effective pressures P_{eff} (i. e. the difference between the confining pressure and the pore pressure).

It should be noted that previous experiments on Leitha limestone (Baud et al., 2017a) have reported a linear relation $\Delta\phi = k\varepsilon$ between the axial strain and porosity reduction over a broad range of conditions. For reference we include in Fig. 3b selected published data on Leitha limestone for porosity reduction versus axial strain. Water-saturated samples of initial porosity 21 and 31% were deformed in drained conditions over a wide range of effective pressures P_{eff} (i.e. the difference between the confining pressure and the pore pressure). In these experiments, $\Delta\phi$ was calculated from the ratio of the pore volume change, inferred from the monitoring of the pore pressure, to the initial bulk volume of the samples (see Baud et al., 2017a for details). There is a trend for the slope k of the data presented in Fig. 3b to increase with increasing effective

265 pressure. For example, for the samples of 21% initial porosity k increased from 0.61 at an
266 effective pressure of 20 MPa to 0.97 at an effective pressure of 60 MPa. It should be emphasized
267 that the global relation $\Delta\phi = k\varepsilon$ applies independent of the failure mode. In particular, since
268 some of these samples have developed CBs and strain localization, this implies that the relation
269 likely applies also to the local porosity and strain at the mesoscopic scale. Such data can
270 accordingly be used to calibrate the partitioning of porosity change (from CT imaging) between
271 axial and transverse strains. In our study, it is particularly simple in that porosity change and
272 axial strain are equal, with negligible transverse strain.

273 To analyze the strain partitioning at the mesoscopic scale, we divided the initial sample into
274 156 layers with a thickness of 65 μm (10 voxels), and determined the local porosity of each layer
275 from the segmented CT image. Such an approach is like treating each layer as a representative
276 element volume at the mesoscopic scale, and the local porosity here corresponds to an average
277 over the volume of each layer. In an experimental context, this is analogous to performing
278 porosimetry measurements on more than one hundred locations in the sample. In the experiment
279 the sample shortened by as much as 20% (Fig. 1); so that we can compare the strains at fixed
280 particle points, we determined the local porosity change $\Delta\phi$ between two scans in each layer,
281 equated it to the local axial strain ε, and then expanded the layer thickness by a factor of 1/(1-ε).
282 This would dilate and adjust the current length of a deformed sample that of the initial sample for
283 comparison.

284 We plot in Fig. 4a the local porosity as a function of the adjusted length at five selected
285 stress states marked (A, B, C, D, E) on Fig. 1. Between A and B, the differential stress increased
286 from 33 MPa to 63 MPa (beyond the first yield point C^*). Comparison of the two profiles

underscores that compaction was unevenly partitioned between the upper and lower parts of the sample. It preferentially developed in a top layer (shaded in gray, corresponding to the cluster of macropores marked in Fig. 2a), where the porosity decreased overall by ~7%. Below this layer, little change of local porosity was observed. Although compaction was significant within the top layer, its porosity profile remained qualitative similar in that six corresponding peaks can be identified in profiles A and B. The absence of compaction localization confirms that the yielding at C^* was associated with the preferential development of distributed compaction in the top layer.

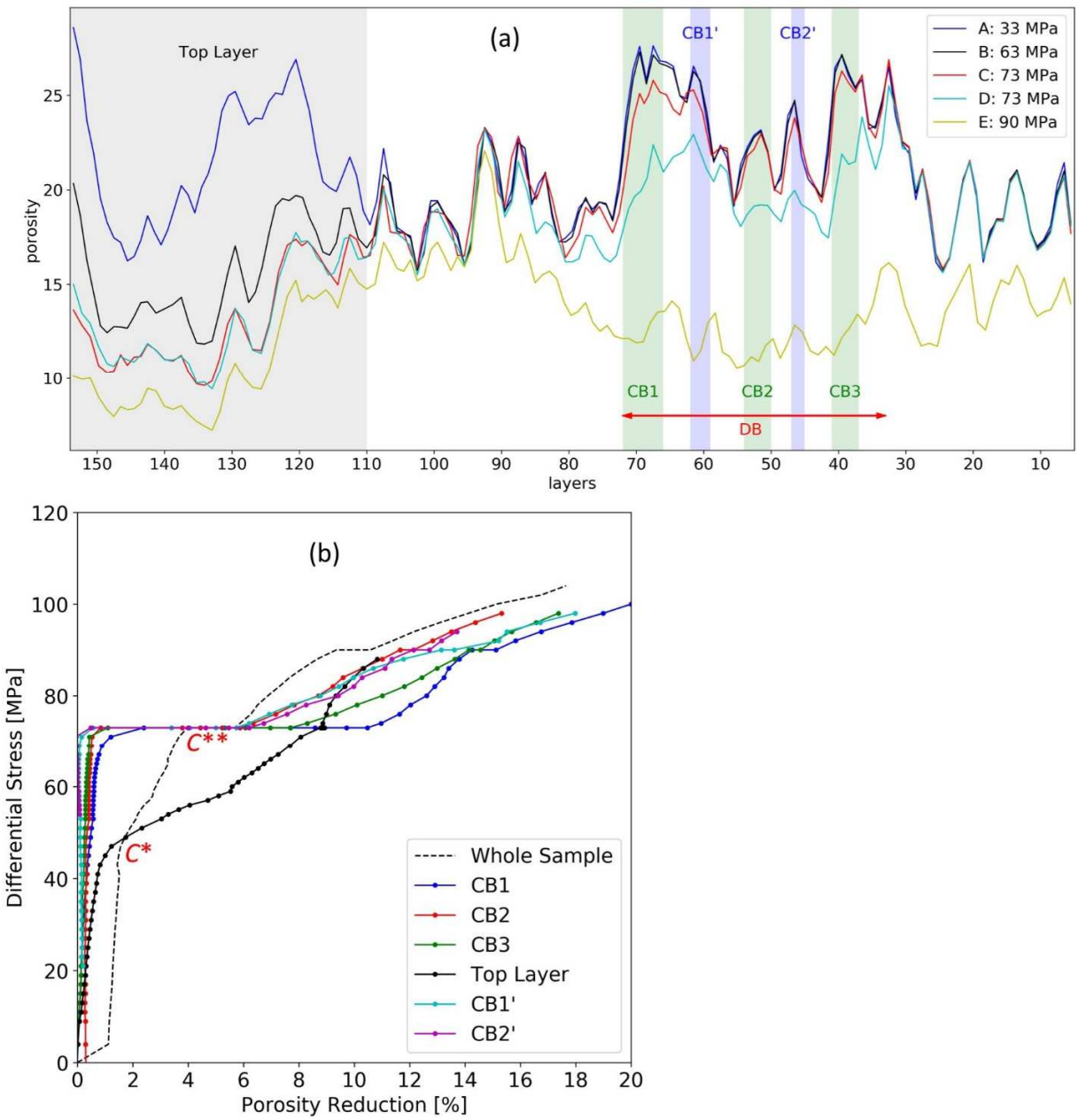


Fig. 4. (a) Local porosity as a function of the µCT layer number in the deformed sample at five stress states (A,B,C,D,E) marked in Fig. 1. The gray shaded area corresponds to the cluster of macropores marked in Fig. 2a. Five compaction bands, CB1, CB2, CB3, CB1' and CB2' are indicated on the graph as green and purple areas. These bands coalesced to form the diffuse compaction band DB indicated by the red arrow. (b) Porosity reductions as function of differential stress for the five compaction bands. For comparison, the global porosity reduction and the porosity reduction in the top layer are also shown as black dashed and solid lines, respectively. For reference, the two yield stresses *C** and *C*** are marked in red.

305 The porosity profile C is for a stress of 73 MPa at the onset of the second yielding *C***.
306 Comparison of profiles B and C shows preferential compaction that persisted within the top
307 layer, with little change of local porosity in the rest of the sample, except for a layer CB1 with
308 appreciable reduction in porosity (Fig. 4a). In the transition from C to D, the sample creeped for
309 several minutes and accumulated a global strain of ~1%. Comparison of the two profiles before
310 and after *C*** shows that compaction had completely shifted to the lower half of the sample, with
311 negligible change in porosity in the top layer. In particular, pronounced compaction had
312 preferentially developed in five layers: CB1 with thickness of 0.39 mm; CB2 and CB3, both of
313 thickness of 0.26 mm; and two relatively thin layers CB1' and CB2' (with thicknesses of 0.20
314 mm and 0.13 mm, respectively). This preferential development of localized porosity at the
315 mesoscopic scale suggests that yielding at *C*** first triggered the nucleation of a discrete
316 compaction band CB1, and the creep deformation was subsequently accommodated by the
317 development of four more discrete bands (CB2, CB3, CB1', CB2'), also visible in the videos S2
318 and S3 presented in supplementary material.

319 Profile E was acquired at a stress of 90 MPa, when the sample had accumulated a strain of
320 ~10% (Fig. 1). Comparison with profile D indicates that a significant fraction of the compaction
321 was observed within the layer DB marked in Fig. 4a, which corresponds to the layer bracketed in
322 Fig. 2. A comparison of profiles A and E also shows that, towards the end of the experiment, the
323 initial heterogeneity in local porosity within layer DB had been smoothed out. The five discrete
324 CBs are embedded within this layer, and our interpretation is that these bands had coalesced to
325 form the diffuse compaction band DB.

326 To characterize quantitatively the partitioning of strain among the top layer and CBs, we
327 plot in Fig. 4b their porosity reduction as function of differential stress. For reference we include

the global porosity reduction and mark the two yield stresses. After the first yielding C^* and before onset of the second yielding C^{**}, the top layer accumulated a local strain of 8%, which represents a global strain of ~2%, comparable to that measured for the whole sample. This corroborates the predominant contribution of the top layer towards compaction during this first stage of yielding. As the sample creeped at a stress of 73 MPa, the five bands CB1, CB2, CB3, CB1' and CB2' had their local porosities reduced by 9%, 6%, 7%, 5% and 5%, respectively (Fig. 4b), which collectively contribute a global strain of about 1%. This constitutes about half of the strain measured for the whole sample, although their thicknesses amount to only one-quarter of the sample length.

As elaborated in the supplementary material, our high-frequency displacement data indicate that, even though the stress level was kept at a nominally constant level during the creep stage, it was actually punctuated by five relatively small stress drops (Fig. S4). We interpret that these stress drops were associated with the nucleation and development of the five discrete CBs, analogous to observations documented extensively in sandstones (Wong and Baud, 2012).

3.3. Spatiotemporal development of damage and micromechanics of failure

Having pinpointed five discrete CBs from our mesoscopic analysis, we next refined the scale to the voxel to further elucidate the spatiotemporal development of these CBs and the associated damage. To quantify the damage we compared two segmented CT images acquired before and after a CB had initiated and propagated across the sample. Between the scans, the deformation of a voxel falls into one of four distinct modes: (1) void to solid, (2) solid to void, (3) solid remains solid, and (4) void remains void. Both modes 1 and 2 could occur only if a voxel had been affected by damage and irreversible displacement. The stress levels and scan numbers we selected for analyzing the five CBs are listed in Table T1 in supplementary material.

For each band, the percentages of voxels with deformation in either mode 1 or mode 2 were evaluated (Table T1).

For the thickest band CB1, between the two scans (at differential stresses of 73 MPa and 82 MPa) the porosity decreased by ~10% (Fig. 4b) which, according to Table T1, corresponds to the trade-off between (mode 1) compaction of 19.7% and (mode 2) dilation of 9.2%. This also implies that altogether 28.9% by volume of CB1 was subjected to either modes of deformation, a proxy for the spatial extent that had been impacted by either compactant or dilatant damage. It should be noted that, because damage in the form of sub-micron microcracking cannot be resolved by our μCT imaging, this percentage likely represents only a lower bound of the damage zone. To highlight the spatial heterogeneity and connectivity of damage, we present in Fig. 5a seven slices along the width of CB1. The damage zone corresponds to the red and blue areas. Our analysis of the spatial distribution and connectivity in the other four bands (Table T1) show that they are qualitatively similar, as illustrated by the 3D images in Fig. 5b.

Whereas this refined analysis delineates details of the spatial distribution of damage on the voxel scale, it has an intrinsic limitation in that little regarding the micromechanical processes is revealed beyond whether they are either compactant or dilatant. Indeed a similar limitation applies also to the measurement of AE as a proxy for damage. In this regard our approach has a distinct advantage because details of the grain-scale deformation were also revealed in the gray-scale images (Fig. 2). We first scrutinized the images at large deformation to track down features that would suggest shear localization cutting through the sample. We were not able to detect inklings of such a development. Focusing on selected regions, we next analyze the time-lapse radiographs (R90) to track the sequential development of pore collapse and CB formation and to infer the micromechanics.

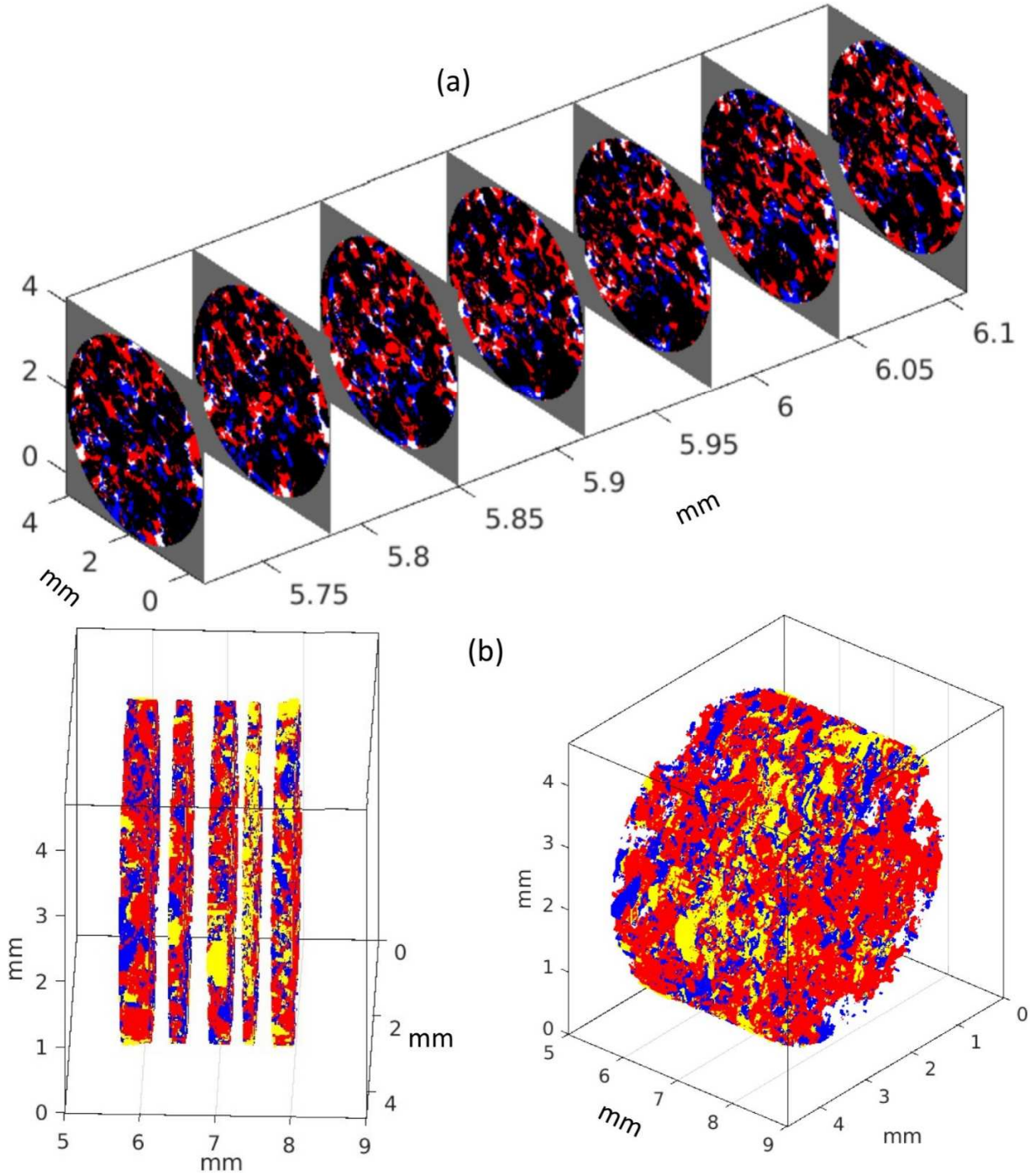


Fig. 5. (a) 3D visualization of damage and porosity reduction in CB1. Seven slices along the width of the band are shown. The voxel-scale deformation falls into four modes (1 compaction: red; 2 dilation: blue; 3 solid; black; 4 void: white). (b) 3D visualizations of damage in the

compaction bands. The voxel-scale deformation falls into four modes (1 compaction: red; 2 dilation: blue; 3 solid: yellow; 4 void: white).

Five time-lapse micrographs of the top layer are shown in Fig. 6. The letter code (a, b, c, d, e) of these figures correspond to the stress states marked in Fig. 6f. Fig. 6a and 6b were acquired at two stresses before *C**; their pore spaces seem almost identical, underscoring that relatively little deformation occurred before the first yield point *C** was reached. The macropore (marked as "M" in Fig. 6b) stands out as one of the largest voids. When the stress increased beyond *C**, significant deformation can be observed (Fig. 6c), preferentially in the vicinity of M. Axial shortening of this macropore was significant, and to accommodate this, compaction developed on either sides of M in the form of grain crushing and collapse of the smaller pores. Where grains impinged on one another, Hertzian fractures initiated and propagated across grains. When a grain was crushed into fragments, some of them fell into the macropore. Beyond the stress state c, the pores continued to contract somewhat, but it can also be seen from Fig. 6d and 6e that compaction in this layer remained distributed.

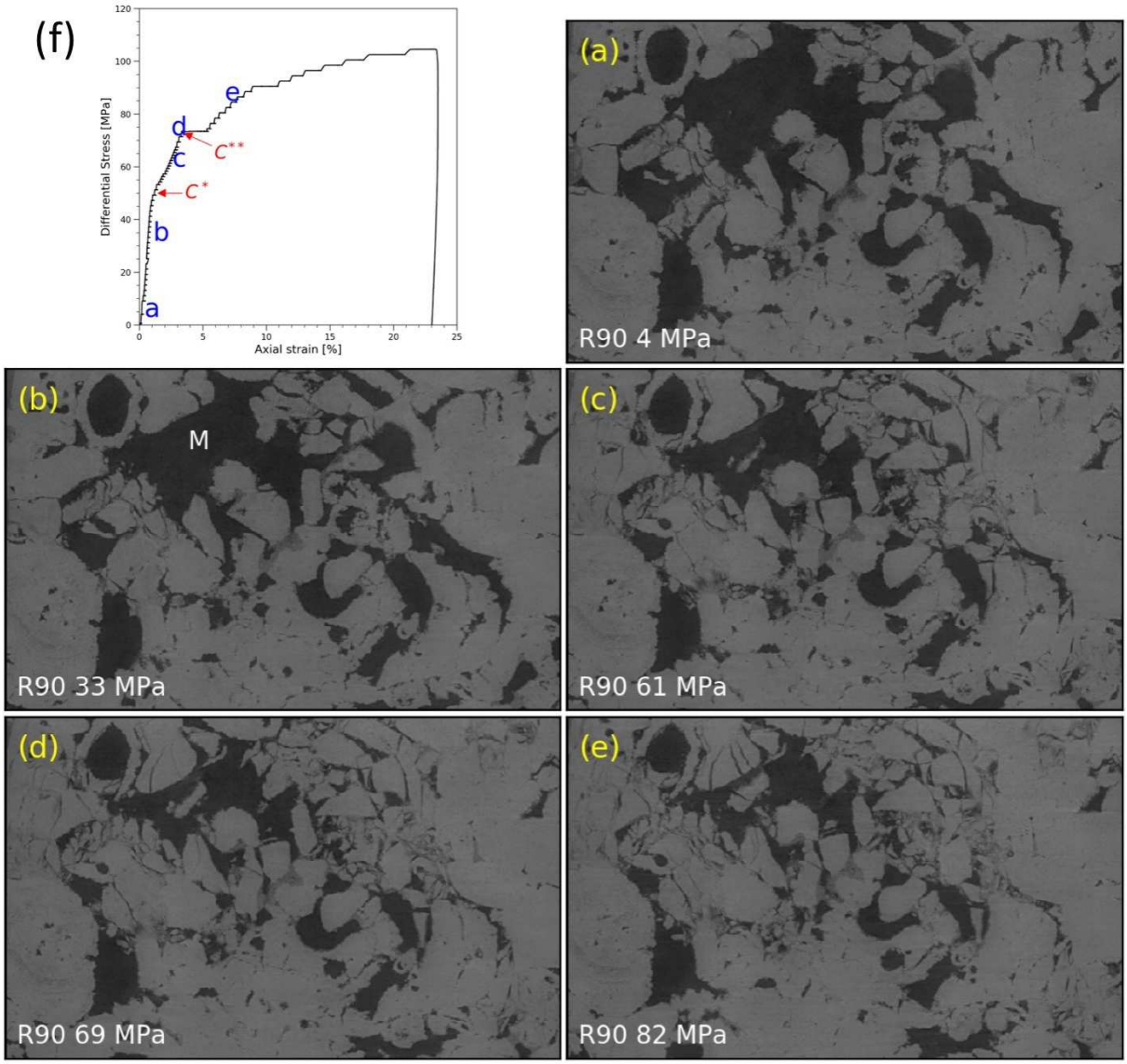


Fig. 6. (a-e) Five micrographs of the top layer of the sample acquired at different levels of stress marked in (f). The width of the micrographs is 4.55 mm. The letter M labels a macropore.

Five time-lapse micrographs of regions that embed CB1, CB2 and CB2 are presented in Fig. 7, Fig. 8, and Fig. 9, respectively. The letter code in these figures correspond to the stress states (a, b, c, d, e) marked in the inset of Fig. 1. Fig. 7a and 7b were acquired at two stresses before *C***, and their pore spaces seem almost identical, showing that relatively little deformation occurred in this region before the second yield point *C*** was reached. However, once *C*** had been attained and the sample creeped for several minutes, significant compaction was observed

(Fig. 7c). Unlike what occurred in the top layer, deformation seemed not to have preferentially developed near the larger pores. Many of the smaller pores had been eliminated, and larger pores had also contracted appreciably. It is likely that grain crushing was pervasive, but the CT images cannot resolve the details. The grain-scale damages were localized in a planar zone aligned along CB1, and at this stage appeared more intense in the right half of the region bracketed by the two dashed lines. In the next stage (Fig. 7d), the damage had spread towards the left as the sample strain hardened. In the last micrograph (Fig. 7e), one can identify a band of damage that cuts through about half of the sample.

In Fig. 8 and Fig. 9, damage evolutions in the other two bands CB2 and CB3 are qualitatively similar to CB1, with the exception that the nucleation sites appeared to be different. For CB2 the compaction appeared to nucleate from near the central region (Fig. 8c) and spread sideways (Fig. 8d), whereas for CB3, it initiated near the center and left side (Fig. 9c), and then spread towards the right (Fig. 9d).

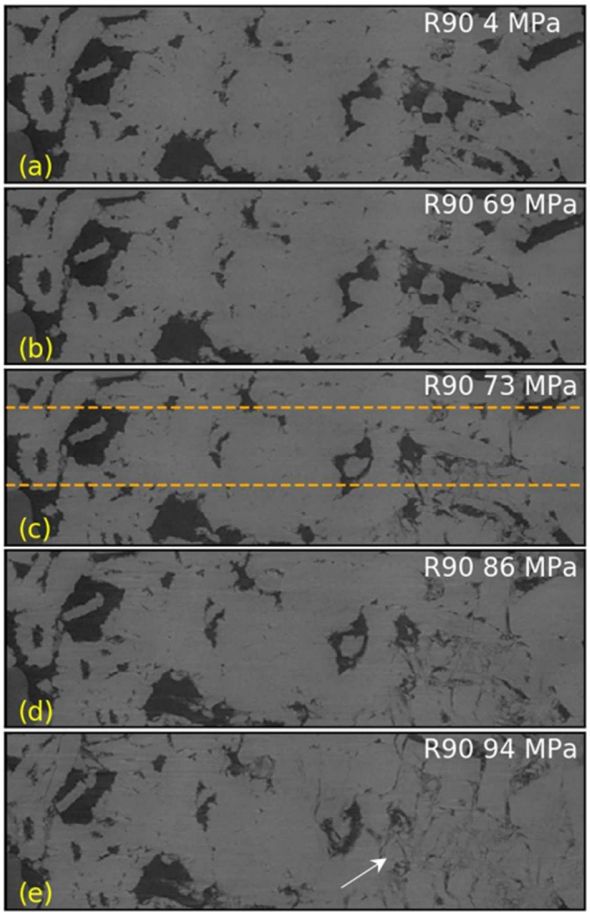


Fig. 7. (a-e) Five micrographs of CB1 acquired at different levels of stress marked in inset of Fig. 1. The width of the micrographs is 4.55 mm. A band of damage is indicated by an arrow in Fig. 7e.

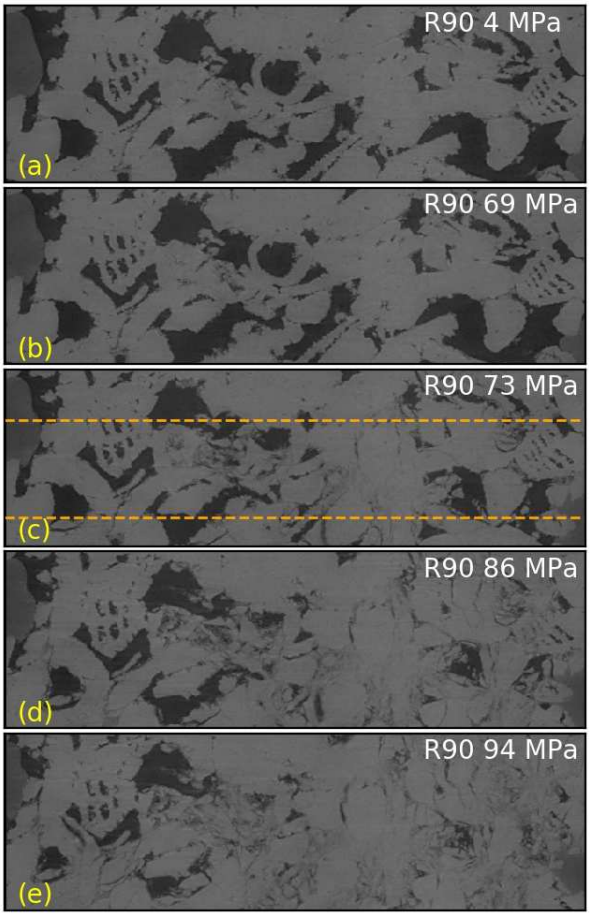


Fig. 8. (a-e) Five micrographs of CB2 acquired at different levels of stress marked in inset of Fig. 1. The width of the micrographs is 4.55 mm.

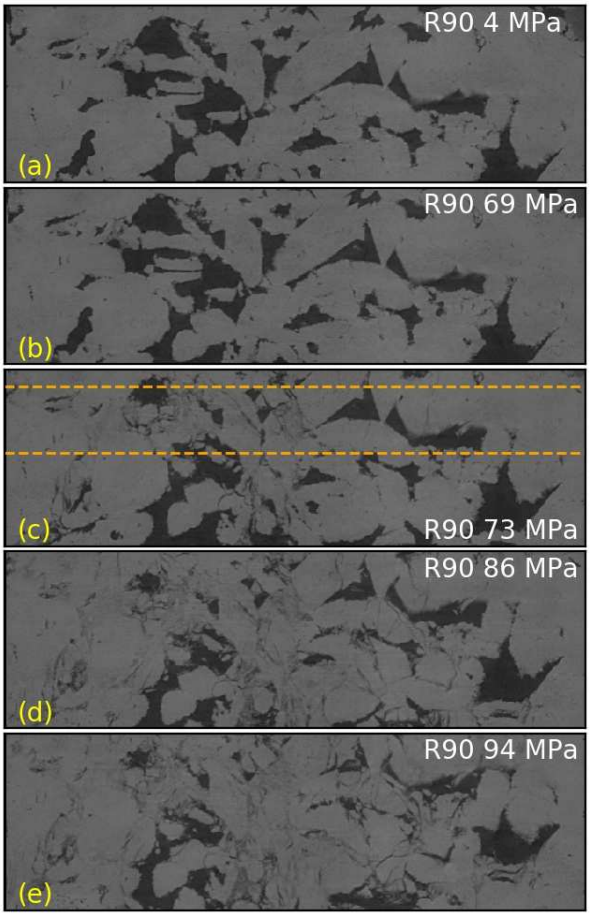


Fig. 9. (a-e) Five micrographs of CB3 acquired at different levels of stress marked in inset of Fig. 1. The width of the micrographs is 4.55 mm

4. Discussion

In this study we conducted a triaxial compression experiment on Leitha limestone in an apparatus that is transparent to the X-ray fluxes of a synchrotron source. With a spatial resolution of 6.5µm, 4D imaging of the sample has allowed us to effectively characterize the progressive development of failure at multiple scales ranging from that of the sample down to the grain. Unlike previous studies that tackled this by imaging deformed samples after multiple loading cycles (e.g., Baud et al., 2015), which is time-consuming and subject to microstructural artifacts

436 from sample unloading, here the research objectives were fully accomplished in one single
437 experiment. In our limestone the mechanical deformation evolved in two stages of yielding
438 manifested by fundamentally different mechanisms. Because the failure did not involve any
439 strain softening or dynamic instability, we were able to elucidate details of its complex
440 development as the sample deformed quasi-statically. To our knowledge this is the first study
441 that has successfully captured using 4D synchrotron X-ray imaging the quasi-static development
442 of compaction strain localization and then failure from the grain to continuum scale in a highly
443 porous carbonate representative of geological reservoir rocks.

444 *4.1. Two stages of yielding in a rock with strong heterogeneity of porosity*

445 Our analysis of strain partitioning at the mesoscopic scale (Fig. 4) indicates that the first and
446 second stages of yielding were associated with distributed and localized compactions in the
447 upper and lower parts of the sample, respectively. The initial yield stress C^* marks the onset of
448 the collapse of a cluster of macropores in the top layer (Fig. 6). It is of interest to note that Baud
449 et al. (2015) inferred a similar behavior in Bleurswiller sandstone, the pore space of which was
450 also highly heterogeneous. They proposed that the initial yield of such a rock would typically
451 involve the collapse of an anomalously porous region, and they furthermore developed a
452 micromechanical model that predicts the initial yield envelope can be approximated by a linear
453 cap. Analogous to our observations here, it was only after the first stage of yielding and the pore
454 space had been homogenized somewhat by the pore collapse that the Bleurswiller sandstone
455 sample progressed to the second yield C^{**}, when discrete compaction bands developed.

456 In their model for initial yield, Baud et al. (2015) analyzed the onset of pore collapse for the
457 idealized case of a spherical pore embedded in a matrix that fails according to the Coulomb
458 criterion. For a dry sample under axisymmetric loading, the yield stress can be expressed as:

459 $$Q = \frac{3(7-5\nu)}{10(2-\nu)}(P^*-P) \qquad (1)$$

460 where Q is the differential stress, P the mean stress, P^* the pressure for the onset of pore collapse
461 under hydrostatic loading, and ν Poisson's ratio. According to Equation (1), the compactant yield
462 envelope in the P-Q space is linear with a slope close to 1 for standard values of Poisson's ratio.
463 To better constrain the initial yield envelope of Leitha limestone for comparison with this model,
464 we performed two additional experiments on dry samples cored from the same block as our
465 sample deformed at the synchrotron. These samples were of larger size (40 mm length and 20
466 mm in diameter). One sample was loaded in conventional triaxial compression at 30 MPa of
467 confining pressure, and the other at a constant differential stress of 4 MPa, following a procedure
468 detailed in Cilona et al. (2014). The mechanical data are presented in Fig. S5, and published
469 mechanical data on compactant yield in porous rocks do not indicate any systematic sample size
470 effects (see for example Tembe et al., 2008). The two new data points bracket the C^* value for
471 our synchrotron experiment (Fig. 1), and altogether the three yield stresses fall on a linear trend
472 with a slope close to 1 (Fig. 10), in agreement with model prediction (1) for ν = 0.2. For
473 reference we include in the figure the corresponding yield envelope and previous data of Baud et
474 al. (2015) on Bleurswiller sandstone, which motivated the elastic-plastic pore collapse model.
475 That this model has been demonstrated to be applicable to porous sandstone and limestone with a
476 relatively heterogeneous pore space suggests that it may be valid for a broad range of porous
477 rocks such similar preexisting heterogeneities in their pore spaces.

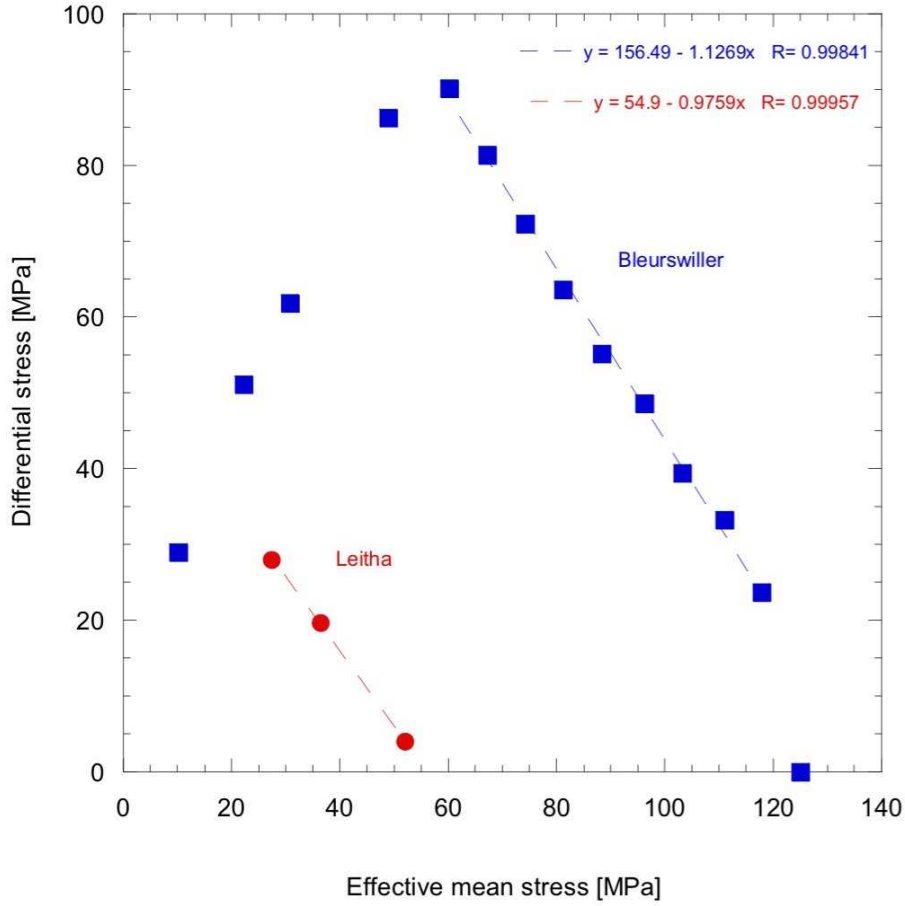


Fig. 10. Comparison between the yield envelopes of Leitha limestone (red circles) and Bleurswiller sandstone (blue squares) from Baud et al. (2015), plotted in the differential stress-effective mean stress space. Linear fits are shown as dashed lines for both envelopes.

4.2. Time-lapse imaging of the dynamics of compaction band formation

Our current understanding of the micromechanics of strain localization derives primarily from AE location and microstructural observation. The former has the intrinsic limitation of being basically kinematic in nature, whereas the latter typically involves post-mortem characterization of damage on multiple samples, which can be difficult to distinguish from artifacts of unloading and sample-to-sample variations. To our knowledge, this is the first study that has circumvented these limitations and successfully captured in details the spatiotemporal evolution of damage related to the dynamics of compaction band formation.

On a continuum scale the dynamics of compaction localization is approximated as a bifurcation phenomenon associated with constitutive instability. On the grain scale, a number of computational micromechanical models (e.g., Wang et al., 2008) have been adopted to predict how the strain localization would initiate and propagate. Our voxel-scale images (Fig. 7, 8, and 9) provide the first time-lapse microstructural observations of the micromechanics of the initiation and propagation of CB formation. As we have shown, the presence of large heterogeneities had a strong impact on the development of stress induced damage in Leitha limestone, particularly in our relatively small sample. It is clear that the presence or absence of such of large heterogeneities would constrain the position of the compaction bands and numerical modelling would need to integrate such complexity to reproduce the results presented here. Here we have focused on the radiographs, but the logical next step is to analyze the 3D complexity of damage development and dynamics of compaction localization using the full set of μCT images and Digital Image Correlation (Renard et al., 2019). An example of such complexity resembles a scenario obtained by Tran et al. (2019) in a rock-like porous material using Digital Image Correlation in which an episode of compaction banding was followed by shear banding**.**

4.3. Compaction localization and time dependent compaction in porous limestone

Since CBs were first observed in sandstone formations, considerable efforts have been made to reproduce such structures in laboratory samples, because of the potential implications for fluid flow at various scales. Series of experimental studies (Baud et al., 2004; Fortin et al., 2005) were successful in producing CBs in cm-size samples. Further analysis revealed that the geometric attributes of field and laboratory CBs follow the same scaling law (Tembe et al., 2008), and that the grain size distribution and porosity are in both cases the key parameters controlling

514 the nucleation of CBs in sandstone (Cheung et al., 2012), in agreement with the discrete element
515 modeling of Wang et al. (2008).

516 Despite the increasing number of field evidence of CBs in limestone formations and of
517 laboratory studies on carbonates, a similar consensus has yet to emerge as far as the occurrence
518 of CBs in porous carbonates is concerned. Laboratory studies showed clearly that compaction
519 localization can occur in limestone (Ji et al., 2015; Baud et al., 2017a), but the link with field
520 observations remains ambiguous. In fact, since field CBs in limestone are often associated with
521 pressure-solution seams (see for example Tondi et al., 2006), one postulate is that chemical
522 processes would be needed to trigger the nucleation of CBs in limestone. In this study, we show
523 unequivocally that this is not the case at least for Leitha limestone. Our 4D μCT data have
524 elucidated the dynamical development of multiple discrete CBs in a dry carbonate. As in
525 sandstone, pore collapse and grain crushing were the main mechanisms that trigger the
526 development of compaction localization.

527 Leitha limestone could be seen as an end-member type of carbonate because this rock is
528 mostly macroporous (Baud et al., 2017a) and its microstructure is somehow similar to that of
529 some sandstones. An outstanding question for future studies would be whether comparable CBs
530 could develop in limestone with dual porosity. This is a difficult challenge since a large part of
531 the pore space would not be visible even at the high resolution used in this study.

532 4D imaging of stress-induced damage in rock based on the method used in this study
533 presents some other limitations beyond resolution related issues. Such technique would not really
534 be efficient if the deformation would occur too fast (because of the incompressible duration of
535 the scans), too slow because of obvious limitations on available beam time, but also if significant
536 time-dependent deformation (creep) would occur during the scanning process. Since previous

studies reported time-dependent deformation in limestone (e.g. Brantut et al., 2014), we decided to perform our experiment in dry conditions. Even so, we observed some creep at several levels of stress, in particular at about 17 MPa of differential stress (Fig. S4). These data show some notable similarities with the creep data on Bleurswiller sandstone presented by Heap et al. (2015). At constant stress (creep conditions), the strain rate decreased but the data were punctuated by episodic changes in strain rate, an indicator of compaction localization. Based on the results of Heap et al. (2015), we can speculate that significant time-dependent compaction driven by stress-corrosion microcracking is also expected in Leitha limestone at stress levels beyond C*. Existing studies on stress corrosion and creep (Atkinson and Meredith, 1987; Brantut et al., 2013) suggest that the resulting strain rates would be strongly influenced in particular by the presence of fluid, fluid chemistry and temperature. In the presence of fluid, CBs could therefore develop in the field at much lower stresses over extended periods of time. At these time scales, other chemical processes should also contribute to the evolution of CB's microstructure.

5. Conclusion

We used *in situ* dynamic synchrotron X-ray imaging to study in real time the development of stress-induced damage associated with inelastic compaction and failure in a porous limestone. Leitha limestone was selected for this study because its pore space is dominated by relatively large macropores with optimum size. Most of the pore space could therefore be resolved in our high resolution images, and no filtering or image analysis was necessary to infer the evolution of the global and local porosity.

To our knowledge this is the first study that has successfully captured the quasi-static development of failure and strain localization from the grain to continuum scale in a limestone reservoir rock. Several conclusions could be drawn from our results:

1) Discrete CBs can develop in a porous limestone, even in dry conditions. The μCT data at the voxel scale elucidate in refined details the nucleation and propagation of discrete CBs under quasi-static loading. The development of CBs involves grain crushing and pore collapse, both visible in our μCT images beyond the yield point.

2) Inelastic compaction of Leitha limestone is characterized, as in some sandstones, by a double yielding behavior. At the onset of shear-enhanced compaction C^*, our μCT images revealed mostly cataclastic pore collapse, while the second yield stress C^{**} was associated with onset of bifurcation and development of discrete CBs.

3) Time-dependent compaction and time-dependent compaction band growth were observed during part of our experiment performed in dry conditions. In the field, CBs could therefore potentially grow in limestone at relatively low stresses over extended period of time.

Acknowledgements

We are most grateful to Ulrike Exner for helping with the sample collection and thank two reviewers whose suggestions greatly improved the manuscript. This study was partially funded by the Hong Kong Research Grants Council GRF 14305714 and GRF14323916, the France-Hong Kong Collaborative Program Procore 30805PM and F-CUHK405/16, the Norwegian Research Council (grant 250661), and CNRS (PICS grant 07961). Beamtime was allocated at the

European Synchrotron Radiation Facility (Long Term Proposal ES-295). Data storage was provided by UNINETT Sigma2 (project NS9073K). The X-ray tomography data will be made available to the scientific community at https://archive.norstore.no/ upon acceptation of the article (Renard, 2019).

References

Anders, M.H., Laubach, S.E., Scholz, C.H., 2014. Microfractures: A review. J. Struct. Geol. 69, 377-394.

Andò, E., Hall, S.A., Viggiani, G., Desrues, J., Bésuelle, P., 2012. Grain-scale experimental investigation of localised deformation in sand: a discrete particle tracking approach. Acta Geotechnica 7 (1), 1-13.

Atkinson, B.K., Meredith, P.G., 1987. Experimental fracture mechanics data for rocks and minerals, in Fracture Mechanics of Rock, edited by B. K. Atkinson, pp. 477-525, Academic Press, London.

Baud, P., Exner, U., Lommatzsch, M., Reuschlé, T., Wong, T.-f., 2017a. Mechanical behavior, failure mode, and transport properties in a porous carbonate. J. Geophys. Res., Solid Earth 122 (9), 7363–7387.

Baud, P., Schubnel, A., Heap, M.J., Rolland, A., 2017b. Inelastic compaction in high-porosity limestone monitored using acoustic emissions. J. Geophys. Res., Solid Earth 122 (12), 9989-10,008.

599 Baud, P., Reuschlé, T., Ji, Y., Cheung, C.S.N., Wong, T.-f., 2015. Mechanical compaction and
600 strain localization in Bleurswiller sandstone. J. Geophys. Res., Solid Earth 120 (9), 6501–6522.

601 Baud, P., Meredith, P.G., Townend, E., 2012. Permeability evolution during triaxial compaction
602 of an anisotropic porous sandstone. J. Geophys. Res. Solid Earth 117 (B5), B05203.

603 Baud, P., Klein, E., Wong, T.-f., 2004. Compaction localization in porous sandstones: Spatial
604 evolution of damage and acoustic emission activity. J. Struct. Geol. 26 (4), 603–24.

605 Brantut, N., Heap, M.J., Baud, P., Meredith, P.G., 2014. Mechanisms of time-dependent
606 deformation in porous limestone. J. Geophys. Res., Solid Earth 119 (7), 5444-5463.

607 Brantut, N., Heap, M.J., Meredith, P.G., Baud, P., 2013. Time-dependent cracking and brittle
608 creep in crustal rocks. J. Struct. Geol. 52, 17-43.

609 Baxevanis, T., Papamichos, E., Flornes, O., Larsen, I., 2006. Compaction bands and induced
610 permeability reduction in Tuffeau de Maastricht calcarenite. Acta Geotech. 1 (2), 123–35.

611 Cheung, C., Baud, P., Wong, T.-f., 2012. Effect of grain size distribution on the development of
612 compaction localization in porous sandstone. Geophys. Res. Lett., 39, L21302.

613 Eichhubl, P., Hooker, J.N., Laubach, S.E., 2010. Pure and shear-enhanced compaction bands in
614 Aztec sandstone. J. Struct. Geol. 32 (12), 1873–86.

615 Fortin, J., Stanchits, S., Dresen, G., Guéguen, Y., 2006. Acoustic emission and velocities
616 associated with the formation of compaction bands in sandstone. J. Geophys. Res., Solid Earth
617 111 (B10), B10203.

618 Fortin, J, Schubnel, A., Guéguen, Y., 2005. Elastic wave velocities and permeability evolution
619 during compaction of Bleurswiller sandstone. Int. J. Rock Mech. Min. Sci. 42 (7-8), 873–89.

620 Fossen, H., Soliva, R., Ballas, G., Trzaskos, B., Cavalcante, C., Schultz, R.A., 2017. A review of
621 deformation bands in reservoir sandstones: geometries, mechanisms and distribution. From:
622 Ashton, M., Dee, S. J. & Wennberg, O. P. (eds) Subseismic-Scale Reservoir Deformation. Geol.
623 Soc., London, Special Publications, 459, https://doi.org/10.1144/SP459.4.

624 Fossen, H., Schultz, R.A., Torabi, A., 2011. Conditions and implications for compaction band
625 formation in the Navajo sandstone, Utah. J. Struct. Geol. 33 (10), 1477–90.

626 Fusseis, F., Steeb, H., Xiao, X., Zhu, W., Butler, I. B., Elphick, S., Mäder, U., 2013. A low-cost
627 X-ray-transparent experimental cell for synchrotron-based X-ray microtomography studies under
628 geological reservoir conditions, J. Synchrotron Rad., 21, 251-253.

629 Heap, M.J., Brantut, N., Baud, P., Meredith, P.G., 2015. Time-dependent compaction band
630 formation in sandstone. J. Geophys. Res., Solid Earth 120 (7) 4808–4830.

631 Ji, Y., Hall, S.A., Baud, P., Wong, T.-f., 2015. Characterization of pore structure and strain
632 localization in Majella limestone by X-ray computed tomography and digital image correlation,
633 Geophys. J. Int. 200, 701-719.

634 Ji, Y., Baud, P., Vajdova, V., Wong, T.-f., 2012. Characterization of pore geometry of Indiana
635 limestone in relation to mechanical compaction. Oil & Gas Science and Technology–Revue de
636 l'IFP Energies Nouvelles 67 (5), 753–75.

637 Lenoir, N., Bornert, M., Desrues, J., Bésuelle, P., Viggiani, G., 2007. Volumetric Digital Image
638 Correlation applied to X-ray microtomography images from triaxial compression tests on
639 argillaceous rock. Strain 43 (3), 193–205.

640 Lockner, D.A., Byerlee, J.D., Kuksenko, V., Ponomarev, A., Sidorin, A., 1992. Observations of
641 quasistatic fault growth from acoustic emissions. In Int. Geophys. 51, 3–31.

642 Louis, L., Wong, T.-f., Baud, P., Tembe, S., 2006. Imaging strain localization by X-ray
643 Computed Tomography: Discrete compaction bands in Diemelstadt sandstone. J. Struct. Geol. 28
644 (5), 762–775.

645 Mirone, A., Brun, E., Gouillart, E., Tafforeau, P., Kieffer, J., 2014. The Pyhst2 hybrid distributed
646 code for high speed tomographic reconstruction with iterative reconstruction and a priori
647 knowledge capabilities. Nuclear Instruments and Methods in Physics Research Section B: Beam
648 Interactions with Materials and Atoms 324, 41–48.

649 Mollema, P.N., Antonellini, M.A., 1996. Compaction bands: A structural analog for anti-mode I
650 cracks in aeolian sandstone. Tectonophysics 267 (1-4), 209–228.

651 Moore, D.E., Lockner, D.A., 1995. The role of microcracking in shear-fracture propagation in
652 granite. J. Struct. Geol. 17 (1), 95–114.

653 Olsson, W.A., Holcomb, D.J., 2000. Compaction localization in porous rock. Geophys. Res. Lett.
654 27 (21). Wiley Online Library: 3537–40.

655 Olsson, W.A. 1999. Theoretical and experimental investigation of compaction bands in porous
656 rock. J. Geophys. Res., Solid Earth 104 (B4), 7219–7228.

657 Passchier, C.W., Trouw, R.A.J., 2005. Microtectonics. Springer Science & Business Media.

658 Paterson, M.S., Wong, T.-f., 2005. Experimental rock deformation-the brittle field. Springer
659 Science & Business Media.

660 Rath, A., Exner, U., Tschegg, C., Grasemann, B., Laner, R., Draganits, E., 2011. Diagenetic
661 control of deformation mechanisms in deformation bands in a carbonate grainstone. AAPG
662 Bulletin 95 (8), 1369–1381.

663 Renard, F., (2019). Synchrotron X-ray imaging in 4D: Multiscale failure and compaction
664 localization in triaxially compressed porous limestone [Data set]. Norstore.
665 https://doi.org/10.11582/2019.00015.

666 Renard, F., McBeck, J., Cordonnier, B., Zheng, X., Kandula, N., Sanchez, J.R., Kobchenko, M.,
667 Noirel, C., Zhu, W., Meakin, P., Fusseis, F., Dysthe, D.K., 2019. Dynamic in situ three-
668 dimensional imaging and digital volume correlation analysis to quantify strain localization and
669 fracture coalescence in sandstone. Pure and applied Geophysics 176 (3), 1083-115.

670 Renard, F., Cordonnier, B., Kobchenko, M., Kandula, N., Weiss, J., Zhu, W., 2017. Microscale
671 characterization of rupture nucleation unravels precursors to faulting in rocks. Earth Planet. Sci.
672 Lett. 476, 69-78, doi: 10.1016/j.epsl.20 17.08.002.

673 Renard, F., Cordonnier, B., Dysthe, D.K., Boller, E., Tafforeau, P., Rack, A., 2016. A
674 deformation rig for synchrotron microtomography studies of geomaterials under conditions down
675 to 10 Km depth in the earth. J. Synchrotron Rad. 23 (4), 1030–1034.

676 Rudnicki, J.W., 2004. Shear and compaction band formation on an elliptic yield cap. J. Geophys.
677 Res., Solid Earth 109 (B3), B03402, 1-10.

678 Schubnel, A., Benson, P.M., Thompson, B.D., Hazzard, J.F., Young, R.P., 2006. Quantifying
679 damage, saturation and anisotropy in cracked rocks by inverting elastic wave velocities. In Rock
680 Damage and Fluid Transport, Part I, 947–73. Springer.

681 Sternlof, K.R., Chapin, J.R., Pollard, D.D., Durlofsky, L.J., 2004. Permeability effects of
682 deformation band arrays in sandstone. AAPG Bulletin 88 (9), 1315–1329.

683 Tembe, S., Baud, P., Wong, T.-f., 2008. Stress conditions for the propagation of discrete
684 compaction bands in porous sandstone. J. Geophys. Res., Solid Earth 113 (B9), B09409.

685 Tondi, E., Antonellini, M.A., Aydin, A., Marchegiani, L., Cello G., 2006. The role of
686 deformation bands, stylolites and sheared stylolites in fault development in carbonate grainstones
687 of Majella Mountain, Italy. J. Struct. Geol. 28, 376-391.

688 Townend, E., Thompson, B.D., Benson, P.M., Meredith, P.G., Baud, P., Young, R.P., 2008.
689 Imaging compaction band propagation in Diemelstadt sandstone using acoustic emission
690 locations. Geophys. Res. Lett. 35 (15), L15301.

691 Tran, T.-P.-H., Bouissou, S., Chemenda, A., Ambre, J., Vacher, P., Michel, P., 2019. Initiation
692 and evolution of a network of deformation bands in a rock analogue material at brittle-ductile
693 transition. Rock Mech. Rock Eng., 52(3), 737-752.

694 Vajdova, V., Baud, P., Wong, T.-f., 2004. Permeability evolution during localized deformation
695 in Bentheim sandstone. J. Geophys. Res., Solid Earth 109 (B10), B10406, 1-15.

696 Wang, B., Chen, Y., Wong, T.-f., 2008. A discrete element model for the development of
697 compaction localization in granular rock. J. Geophys. Res., Solid Earth, 113, B03202,
698 doi:03210.01029/02006JB004501.

699 Wong, T.-f., Baud, P., 2012. The brittle-ductile transition in porous rock: A Review. J. Struct.
700 Geol. 44, 25–53.

701 Wong, T.-f., Baud, P., Klein, E., 2001. Localized failure modes in a compactant porous rock.
702 Geophys. Res. Lett. 28 (13), 2521–2524.

703 Wong, T.-f., 1982. Micromechanics of faulting in Westerly granite. Int. J. Rock Mech. Min. Sci.
704 Geomechanics Abstracts 19, 49–64.

705 Zang, A., Wagner, F.C., C., Stanchits, S., Janssen, C., Dresen, G., 2000. Fracture process zone in
706 granite. J. Geophys. Res., Solid Earth 105 (B10), 23651–23661.

707 Zhao, Q., Tisato, N., Kovaleva, O., Grasselli, G., 2018. Direct observation of faulting by means
708 of rotary shear tests under X‐ray micro‐computed tomography. J. Geophys. Res.: Solid Earth
709 123 (9), 7389-7403.